Velocity and attenuation in partially saturated rocks: poroelastic numerical experiments

Hans B. Helle,[1]* Nam H. Pham[2]† and José M. Carcione[3]

[1]*Norsk Hydro a.s., PO Box 7190, 5020 Bergen, Norway*, [2]*Department of Petroleum Engineering and Applied Geophysics, Norwegian University of Science and Technology, 7491 Trondheim, Norway, and* [3]*Istituto Nazionale di Oceanografia e di Geofisica Sperimentale (OGS), Borgo Grotta Gigante 42C, 34010 Sgonico, Trieste, Italy*

ABSTRACT

We use a poroelastic modelling algorithm to compute numerical experiments on wave propagation in a rock sample with partial saturation using realistic fluid distribution patterns from tomography scans. Frequencies are in the range 10 to 500 kHz. The rock is a homogeneous isotropic sandstone partially filled with gas and water, which are defined by their characteristic values of viscosity, compressibility and density. We assume no mixing and that the two different pore-fills occupy different macroscopic regions. The von Kármán self-similar correlation function is used, employing different fractal parameters to model uniform and patchy fluid distributions, respectively, where effective saturation is varied in steps from full gas to full water saturation.

Without resorting to additional matrix–fluid interaction mechanisms, we are able to reproduce the main features of the variation in wave velocity and attenuation with effective saturation and frequency, as those of published laboratory experiments. Furthermore, the behaviour of the attenuation peaks versus water saturation and frequency is similar to that of White's model. The conversion of primary P-wave energy into dissipating slow waves at the heterogeneities is shown to be the main mechanism for attenuating the primary wavefield. Fluid/gas patches are shown to affect attenuation more than equivalent patches in the permeability or solid-grain properties.

INTRODUCTION

The primary goals of seismic exploration are the identification of pore fluids and the mapping of hydrocarbon deposits. In the area of hydrocarbon field reservoir management, recent developments in borehole acoustic measurements and subsea geophone arrays make it feasible to conduct high-resolution surveys to detect pockets of unswept reserves and to monitor the progress of enhanced recovery by gas and water injection. Understanding the physics of elastic waves in porous rocks

partially filled with gas and liquid is thus important for exploring and exploiting hydrocarbon reservoirs.

Regions of non-uniform patchy saturation occur at gas–oil and gas–water contacts in hydrocarbon reservoirs. Also, during production, gas may come out of solution and create pockets of free gas. When laboratory measurements and sonic logs are used to infer the acoustic properties at seismic frequencies, the frequency dependence of these properties becomes a key factor. As demonstrated by White (1975), wave velocity and attenuation are substantially affected by the presence of partial (patchy) saturation, depending mainly on the size of the gas pockets (saturation), frequency, permeability and porosity of rocks.

Patchy saturation effects on acoustic properties have been observed by Murphy (1984) and Knight and

Nolen-Hoecksema (1990). Cadoret, Marion and Zinszner (1995) have observed the phenomenon in the laboratory in the frequency range 1–500 kHz. Two different saturation methods result in different fluid distributions and produce two different values of velocity for the same saturation. Imbibition by depressurization produces a very uniform saturation, while drainage by drying produces heterogeneous saturation at high water-saturation levels. In the latter case, the experiments show considerably higher velocities, as predicted by White's (1975) theory. The experimental results of Yin, Batzle and Smith (1992) at 2 kHz display consistent peaks in resonance attenuation at high water saturation. A strong dependence on the saturation history is evident, with the attenuation peak located at 90% water saturation in the drainage experiment, and 98% water saturation for imbibition techniques. Similar features have been reported by Bourbie and Zinszner (1984) at 500 kHz and Cadoret, Mavko and Zinszner (1998) at 1 kHz.

A number of theories have predicted the effects of fluids on attenuation and seismic velocities at full saturation (e.g. Biot 1962; O'Connell and Budiansky 1977) while fewer theories address partial saturation (e.g. White 1975). Although attenuation still remains poorly understood and underexploited, it is believed by many investigators that in the seismic and sonic frequency range (10 Hz–20 kHz), the dominating mechanisms of wave attenuation are oscillating flow of the viscous pore fluid and the grain boundary friction (Winkler and Nur 1979, 1982). The role of pore fluid in controlling the velocity was well established in the low-frequency (seismic) limit by Gassmann (1951), and for ultrasonic frequencies (0.5 MHz and above) by the experimental studies of Gregory (1976), Domenico (1977) and others. The few published results obtained in the sonic frequency band (1–20 kHz), e.g. by Murphy (1984) and Cadoret *et al.* (1995), are usually in relatively good agreement with the Gassmann model. For higher frequencies (50 kHz and above), the velocity versus water saturation relationship is more complex and depends strongly on rock type and porosity (Gregory 1976). Heterogeneity of the rock material (Lucet and Zinszner 1992) and fluid distribution (Cadoret *et al.* 1995, 1998) seem to be important factors in explaining the observed behaviour of elastic waves at sonic and ultrasonic frequencies.

White's (1975) model describes wave velocity and attenuation as a function of frequency, permeability and porosity, among other parameters. Attenuation and velocity dispersion are caused by fluid flow between the water phase and the gas pockets, which have different pore pressures. The critical fluid diffusion relaxation scale is proportional to the square root of the permeability-to-frequency ratio (e.g. Mavko, Mukerji and Dvorkin 1998, p. 207). At seismic frequencies, the length scale is very large, and the pressure is nearly uniform throughout the medium, but as frequency increases, pore pressure differences can cause an important increase in P-wave velocity. White's model considers spherical gas pockets located at the centre of a cubic array saturated with liquid. For simplicity in the calculations, White considered two concentric spheres, where the volume of the outer sphere is the same as the volume of the elementary cube. The theory provides an average of the bulk modulus for a single gas pocket, without taking into account the interactions between neighbouring gas pockets. Gist (1994) successfully used White's model to fit ultrasonic velocities obtained from saturations established using drainage techniques. He used saturation-dependent moduli as input to White's model instead of the dry-rock moduli. The predicted velocities, considering local fluid flow, are higher than the velocities predicted by White's model. Recently, Johnson (2001) developed a generalization of White's model for patches of arbitrary shape. This model has two geometrical parameters besides the usual parameters of Biot's theory: the specific surface area and the size of the patches. The model was used by Tserkovnyak and Johnson (2002) to determine the characteristic patch size as a function of water saturation from the dispersion and attenuation data of Cadoret *et al.* (1995, 1998).

Numerical simulations, based on the full-wave solution of the poroelastic equations, can be useful to study the physics of wave propagation in partially saturated rocks. Although White's (1975) model is an ideal representation of patchy saturation, its predictions are qualitatively correct, and serve as a reference theoretical framework. However, Biot's (1962) theory provides the only existing treatment of the problem that directly relates acoustic velocity and attenuation to measurable macroscopic characteristics of a rock. In this sense, it is useful to compare the results of White's model with numerical simulations based on Biot's theory of poroelasticity as made in a recent study by Carcione, Helle and Pham (2003). This analysis confirms that Biot's theory shows more dissipation and higher velocities than White's model due to multiple scattering of slow waves and local fluid-flow effects.

In the present investigation, a more realistic situation is considered, where an arbitrary (general) pore-scale fluid distribution is modelled. By using computerized tomography (CT) scans, it is possible to visualize the fluid distribution in real rocks (Cadoret *et al.* 1995). Fractal models, such as the von Kármán autocovariance function, calibrated by the CT scans, are used to model realistic fluid distributions. We introduce

a numerical rock sample with homogeneous rock properties, but with alternately uniform and patchy fluid distributions, based on a fractal model utilizing the CT scans of Cadoret *et al.* (1995). Using numerical simulations of poroelastic wave propagation in the frequency range 10–500 kHz, we investigate the effect of varying the fluid distribution patterns and effective saturation. By analysing the recorded wave arrivals, we obtain values of velocity and attenuation versus effective fluid saturation that are consistent with published laboratory measurements. Visual inspection of the numerical wavefield reveals that the attenuation of the primary wave can be explained by slow-wave conversion at the saturation heterogeneities. For comparison, we substitute the gas pockets with material inclusions of equivalent seismic contrast, but otherwise the same homogeneous permeability and porosity, fully saturated with water. Finally, we include patches of low-permeability rock coinciding with the gas pockets, embedded in a high-permeability water-saturated background. Heterogeneities in gas/fluid distribution are shown to be more effective in attenuating the primary wavefield than those of equivalent heterogeneities in rock material and permeability.

We solve the poroelastic equations with an algorithm developed by Carcione and Helle (1999), which uses a 4th-order Runge–Kutta time-stepping scheme and the staggered Fourier method for computing the spatial derivatives. The stiff part of the differential equations is solved with a time-splitting technique, which preserves the physics of the quasi-static slow wave at low frequencies.

In general, P-wave and S-wave velocities can be higher in partially saturated rocks than in dry rocks. As predicted by White's (1975) model, this behaviour depends on frequency, viscosity and permeability. It is therefore important to investigate the sensitivity and properties of wave velocity and attenuation versus pore-fluid distribution. This is the basis for direct hydrocarbon detection and enhanced oil recovery and monitoring, since techniques such as 'bright spot' and AVO analyses make use of those physical properties. The modelling methodology used in the present study constitutes a powerful computational tool to investigate the physics of wave propagation in porous rocks, and, in some cases, can be used as an alternative method to laboratory experiments.

NUMERICAL ROCK WITH FRACTAL FLUID/GAS DISTRIBUTION

The numerical rock sample is a homogeneous isotropic Berea sandstone with a porosity of 24.6% and permeability of 0.55 darcy (King, Marsden and Dennis 2000), partially filled

Table 1 Material properties of the single constituents

Solid	Bulk modulus, K_s	35.0 GPa
	Shear modulus, μ_s	35.0 GPa
	Density, ρ_s	2650 kg/m^3
Matrix	Bulk modulus, K_m	9.25 GPa
	Shear modulus, μ_m	9.25 GPa
	Porosity, ϕ	0.246
	Permeability, κ	0.55 D
	Tortuosity, T	2.5
Gas	Bulk modulus, K_g	0.01 GPa
	Density, ρ_g	100 kg/m^3
	Viscosity, η_g	0.02 cP
Water	Bulk modulus, K_w	2.4 GPa
	Density, ρ_w	1000 kg/m^3
	Viscosity, η_w	1.0 cP

Table 2 Properties of the saturated rock

	Water-filled	Gas-filled
ρ	2244 kg/m^3	2023 kg/m^3
$c_{P_+}(0)$	3418 m/s	3268 m/s
$c_{P_+}(\infty)$	3434 m/s	3275 m/s
$c_{P_-}(0)$	44 m/s	23 m/s
$c_{P_-}(\infty)$	813 m/s	195 m/s
$f_{peak}(P_+)$	27.79 kHz	5.56 kHz

with water and gas. The properties of the rock and pore-filling fluids are given in Table 1. No mixing is assumed and the two different pore-fills occupy different macroscopic regions of the model. In Table 2, we give the bulk properties of the rock, fully saturated with a single fluid, gas or water, respectively, where the relaxed ($f = 0$) and unrelaxed ($f = \infty$) phase velocities of the fast compressional wave (c_{P_+}) and the slow wave (c_{P_-}) are given. Also listed is the central frequency of the dominant attenuation peak (f_{peak}) corresponding to the Biot peaks for the rock, fully saturated with gas or water, respectively.

Statistically, seismic heterogeneity is often characterized by the so-called von Kármán self-similar correlation function, commonly cited in turbulence theory and given by

$$N(r) = \frac{1}{2^{m-1}\Gamma(m)} \left(\frac{r}{l}\right)^m \mathcal{K}_m\left(\frac{r}{l}\right), \tag{1}$$

where r is the lag, l is the correlation length, Γ is the gamma function and $\mathcal{K}_m$ is the modified Bessel function of the second

kind. Following Frankel and Clayton (1986), we consider a specific type of von Kármán function where $m = 0$ and

$$N(r) = \mathcal{K}_0 \left(\frac{r}{l} \right). \tag{2}$$

The corresponding wavenumber-domain correlation function is

$$P(k_x, k_z) = \Lambda \left(1 + k_r^2 l^2 \right)^{-(\nu + \mathcal{E}/2)}, \tag{3}$$

where $k_r = (k_x^2 + k_z^2)^{1/2}$ is the radial wavenumber, ν ($0 < \nu < 1$) is a self-similarity coefficient, Λ is a normalization constant, and $\mathcal{E}$ is the space dimension. If $\nu = 0$, the function has pure fractal behaviour, and if $\nu = 0.5$, the exponential correlation function is obtained. The von Kármán correlation function describes self-affine, fractal processes of fractal dimension $\mathcal{D} = \mathcal{E} + 1 - \nu$ at scales smaller than l. For a 2D model, $\mathcal{E} = 2$ and $\mathcal{D}$ thus lies between 2 for very smooth fluctuations and 3 for very complex fluctuations (Holliger 1997). Here, we set $\mathcal{D} = 2$ and vary the fractal correlation parameter l to generate models with uniform and patchy fluid distribution, respectively, using small values of l for uniform saturation and larger values for patchy saturation. For modelling the patchy distribution, we set the correlation length $l = l_p$, expressed by

$$l_p(S_w) = \gamma_1 + \gamma_2 \exp \left(\gamma_3(|S_w - 0.5| + 0.5) \right), \tag{4}$$

to account for the fact that patches are more pronounced at high and low values of saturation S_w than in the intermediate range. The factors γ_i are estimated from the CT scans, and to estimate the correlation length in the case of uniform distribution $l = l_u$, we simply determine the ratio l_u/l_p by comparing the corresponding CT images. For models used in this study, we have determined the following values for the coefficients of (4): $\gamma_1 = 3 \times 10^{-4}$ m, $\gamma_2 = 6 \times 10^{-8}$ m, $\gamma_3 = 10$ and $l_u/l_p = 0.3$.

To construct the fluid distribution of a given effective water saturation $S_w \in [0,1]$ on the 2D numerical grid, we adopted the following procedure: Firstly, a random number generator assigned a value between zero and one, sequentially, to each gridpoint. The random field was then Fourier transformed to the wavenumber domain, filtered by (3) to obtain the desired spectrum, transformed back to the spatial domain and normalized to the interval $P \in [0,1]$ to yield the saturation field for the simulations. Secondly, to design effective saturation values for the numerical rock, where each gridpoint is assigned pure water or pure gas, we introduce a control parameter $\Omega \in [0,1]$ such that for each gridpoint we assign water if $P < \Omega$ and gas if $P \geq \Omega$. For example, for 100% gas saturation ($S_w = 0$), we set $\Omega = 0$ and for 100% water ($S_w = 1$), we set $\Omega = 1$. For
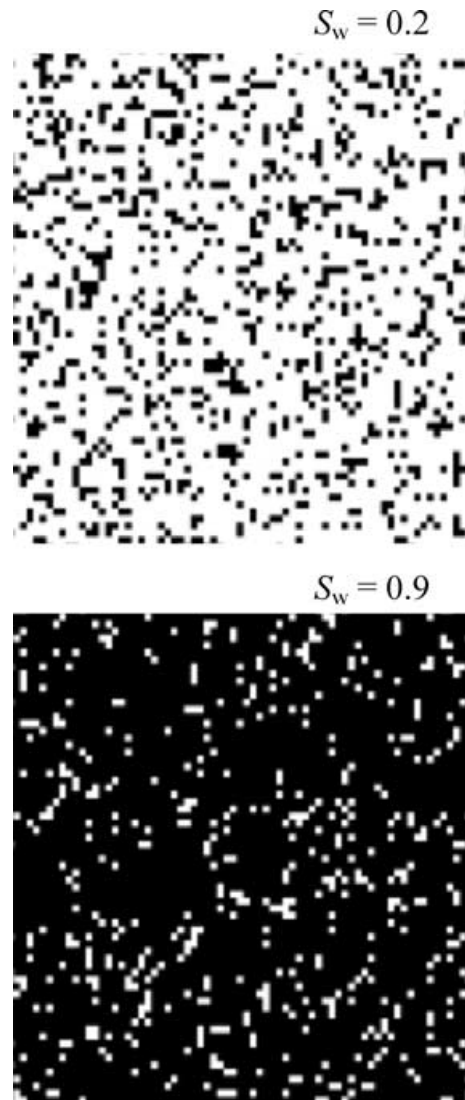
Figure 1 Examples of uniform distribution of fluid for $S_w = 0.2$ (top) and $S_w = 0.9$ (bottom) in a 70×70 mm rock sample. Water and gas are indicated by black and white, respectively. Grid size is 1 mm. Fractal correlation length is $l_u \approx 0.25$ mm and patch dimension is in the range 1–5 mm.

$\Omega = 0.5$ we obtain S_w around 0.5, but the exact value remains to be determined by point-counting the grid as was done for the CT scans by Cadoret *et al.* (1995). Examples of the resulting distribution of gas and water for uniform and patchy saturation are shown in Figs 1 and 2, respectively.

PHASE VELOCITY AND ATTENUATION

The concept of complex velocity can be used to obtain the phase velocity and attenuation factor (e.g. Carcione 2001,
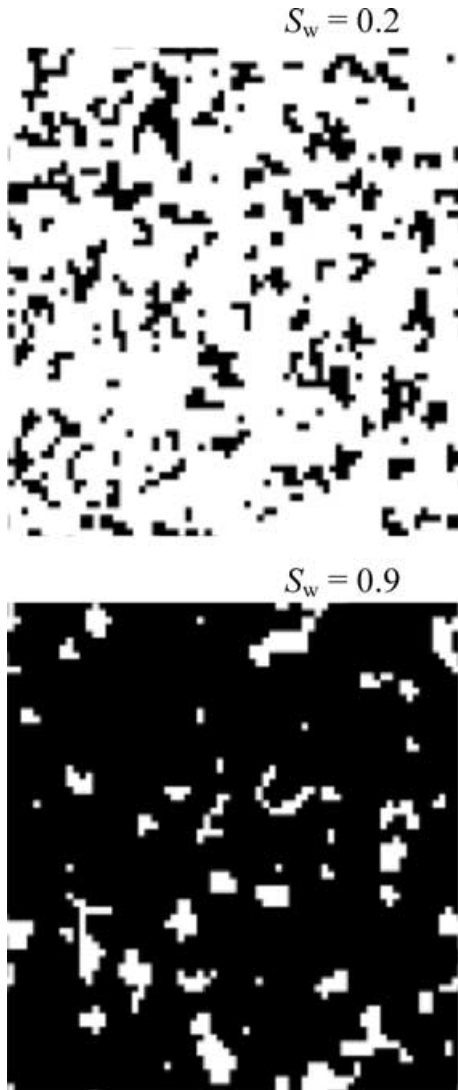
Figure 2 Same parameters as in Fig. 1 but for patchy distribution. Fractal correlation length is $l_p \approx 1$ mm and patch dimension is in the range 1–12 mm.

factor can be expressed as

$$Q = \frac{\mathrm{Re}(v^2)}{\mathrm{Im}(v^2)}. \tag{7}$$

[Otherwise, the Q factor for porous media has a more complex expression (Carcione 2001, p. 289).] The relationship between the attenuation factor and the quality factor Q can be expressed as

$$\alpha = \frac{2\pi f}{c}(\sqrt{Q^2 + 1} - Q) \approx \frac{\pi f}{cQ}, \tag{8}$$

where $f = \omega/(2\pi)$ is the frequency (Carcione 2001, p. 139). The second relationship on the right-hand side holds for low-loss solid ($Q \gg 1$).

Determination of velocity and attenuation is based on the recorded wave arrivals in three equidistant circular arrays of points within the model, centred at the source location as shown in Fig. 3. While recordings from R_1 and R_3 are the main data for the analysis, the middle receiver R_2 is used for verification (Fig. 4). The phase velocity in the numerical experiments is computed from the centre of gravity of $|\mathbf{v}|^2$ versus propagation time, where $\mathbf{v}$ is the bulk particle-velocity field (Carcione 1996). The numerical phase velocity is estimated by averaging the velocities obtained at the five receivers R_3. More details about this calculation are given in Carcione,
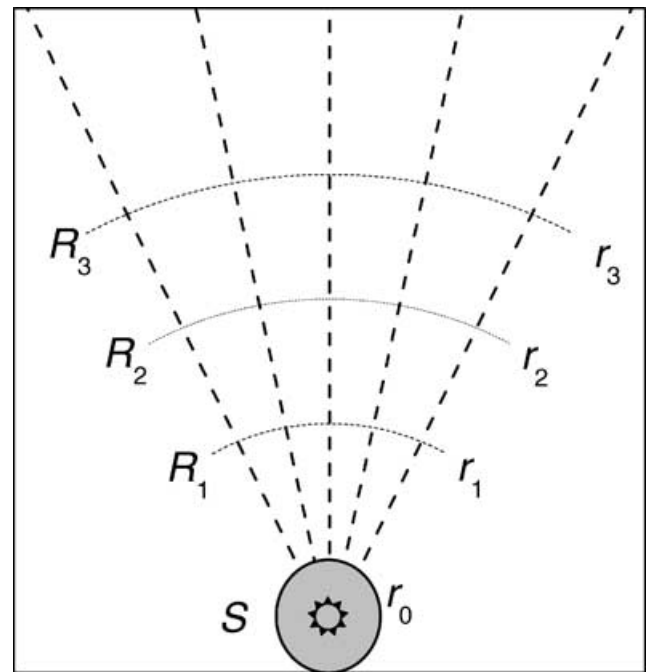
p. 55). Let v be the P-wave complex velocity obtained with White's (1975) model. Then the phase velocity and attenuation factor are given by

$$c = \left[\mathrm{Re}\left(\frac{1}{v}\right)\right]^{-1} \tag{5}$$

and

$$\alpha = -\omega\, \mathrm{Im}\left(\frac{1}{v}\right), \tag{6}$$

respectively, where ω is the angular frequency. If we approximate the porous medium by a viscoelastic solid, the quality

Figure 3 Source (S) and receiver (R_i) geometry used for recording the transmitted wavefield. A circular region of radius r_0 surrounding the source is fully water saturated to assure a uniform initial wavefront.

Quiroga-Goode and Cavallini (1996) and Carcione (2001, p. 145). The determination of phase velocity in terms of the location of the energy is justified from the fact that for isotropic media and homogeneous viscoelastic waves, the phase velocity is equal to the energy velocity (Carcione 2001, p. 99).
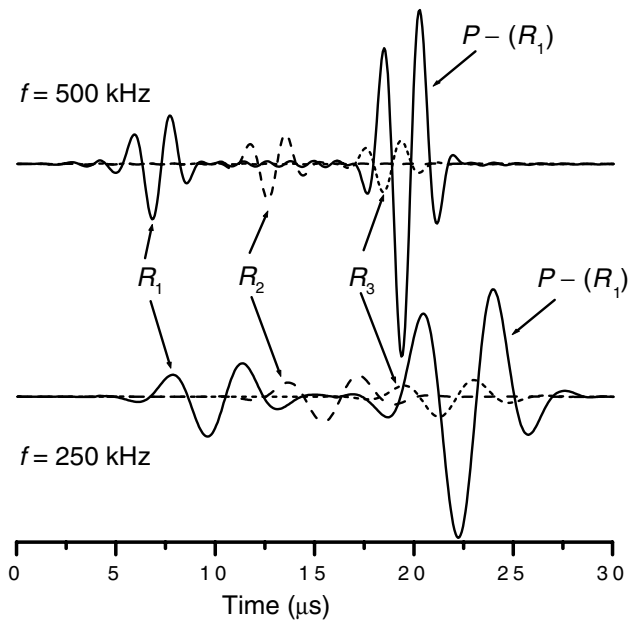

Figure 4 Examples of recorded fluid pressure of fast P-wave (P_+) arrivals at the three receiver locations R_1, R_2 and R_3 (Fig. 3) for 250 kHz and 500 kHz. The slow P-wave (P_-) recorded at R_1 is the dominating event. Fully water saturated ($S_w = 1$).

To estimate attenuation, we use the classical spectral ratio approach discussed by Toksöz, Johnston and Timur (1979), implying that the amplitude ratio A_1/A_3 at the dominant frequency f (Fig. 5) satisfies

$$\ln\left[\frac{A_1(f, r_1)}{A_3(f, r_3)}\right] = \alpha(r_3 - r_1) + \ln\left(\frac{G_1}{G_3}\right), \tag{9}$$

where r_i denotes the source–receiver radial distances, and G_i denotes the respective geometrical spreading factors. Using relationship (8), equation (9) can be rewritten as

$$\ln\left[\frac{A_1(f, r_1)}{A_3(f, r_3)}\right] = \frac{\pi f(r_3 - r_1)}{Qc} + \ln\left(\frac{G_1}{G_3}\right). \tag{10}$$

The quality factor is determined from the slope of the line fitted to $\ln(A_1/A_3)$.

WAVE SIMULATION AND ANALYSIS OF THE WAVEFIELDS

The objective of this study is to determine from numerical experiments the wave velocity and attenuation as a function of water saturation S_w and dominant wave frequency f. The frequencies used in the experiments and the corresponding numerical grids are listed in Table 3. We consider a regular grid where the size and grid spacing are adjusted to the wave frequency. For the high frequencies (250–500 kHz), a small numerical grid consisting of 198×198 ($n_x \times n_z$) points at $\Delta x = 0.5$ mm spacing is sufficient. For the low frequency of 10 kHz (long wavelength), we expanded the model to 804 points at 2 mm spacing in the primary direction (z) to
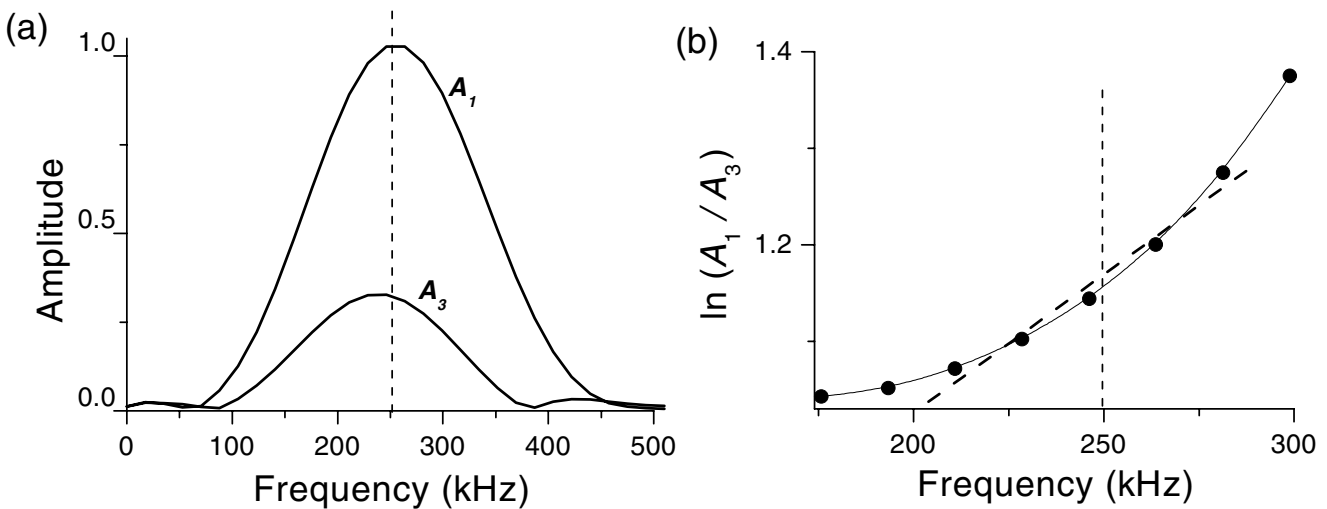

Figure 5 Examples of amplitude spectra of the 250 kHz fast P-wave arrivals at the receiver locations R_1 and R_3 (a) and the corresponding spectral ratio (b) for estimating the attenuation.

Table 3 Numerical parameters for the wave simulations

f (kHz)	$\Delta x = \Delta z$ (mm)	n_x, n_z	n_a	Δt (ns)	n_t	r_0	r_1	r_2	r_3
500	0.5	198	30	62	500	23	28	68	108
250	0.5	198	30	62	500	23	28	68	108
125	1	208	30	124	550	30	32	70	108
100	1	208	30	124	550	30	32	70	108
75	1	420	60	163	850	60	64	142	220
50	1	420	60	163	850	60	64	142	220
10	2	495, 840	120	444	1800	150	152	280	410

allow for a sufficiently long travelpath and record length n_t for the wave analysis. The source is a Ricker wavelet applied to the bulk material, with a dominant frequency f. A circular region of radius r_0 (Fig. 3) surrounding the source is fully water saturated to assure a uniform initial wavefront. Since the source is radially symmetrical and the matrix is homogeneous and isotropic, no S-waves are generated. The wavefield is computed with a time step Δt varying from 62 to 444 ns, within the limits of numerical stability for the grid size used. Absorbing boundaries of width n_a points have been applied at the borders of the mesh, using an exponential damper to prevent wavefield wraparound from interfering with the primary wavefield at the receiver locations. In a fan-shaped distribution along five rays centred at the source (Fig. 3), receivers are located at distances r_1, r_2 and r_3, given in terms of gridpoints in Table 3.

Comparison of the wavefields (bulk and fluid pressure) after 300 time steps for the uniform and the patchy models, with $S_w = 0.9$ and $f = 500$ kHz, are shown in Fig. 6. We identify the primary P-wave front at the top edge of the model and the dominant slow-wave front encircling the source location. In the uniform model, we see cascades of small-scale events displaying the character of scattering diffractions. In the patchy model, we identify the majority of these diffracting events as slow waves generated when the primary P-wave front intersects the fluid discontinuities. The latter is well expressed by the details displayed in Fig. 6(c) where the primary P-wave is seen to excite slow waves when intersecting the gas pockets, leaving a cascade of slow waves in its tail. Multiple scattering within the gas pockets also constitutes important events affecting the primary wavefield as discussed in more detail by Carcione *et al.* (2003). Significant events identified as mode conversion from slow to fast P-waves can also be seen. Snapshots at the same instant and with the same models, but for $f = 250$ kHz, are shown in Fig. 7. Here, the above features are essentially repeated but with twice the wavelength of the former simulation. Moreover, the primary wavefront has travelled a shorter distance during the same time interval as it is apparent in the micro-seismograms of Fig. 4.

The velocity and attenuation estimated as a function of saturation, for the range of frequencies, are shown in Figs 8 and 9, respectively. In general, the velocities for the patchy models are significantly higher than those for the uniform models, in qualitative agreement with White's (1975) theory (see Carcione *et al.* 2003) and published experimental data of e.g. Cadoret *et al.* (1995). For the lower frequency range, the value of c_{P_+} is slightly above the Gassmann lower bound (for $f = 0$), and for the high-frequency range, the values are below the upper bound, here indicated by the velocity at 500 kHz predicted by the empirical model of Brie *et al.* (1995), and modified by Pham *et al.* (2002) to account for a frequency-dependent fluid bulk modulus. In general, the behaviour of c_{P_+} versus S_w is in fair agreement with the published laboratory data. The initial decline in c_{P_+} at low S_w for all frequencies in the case of uniform saturation agrees with the results of Cadoret *et al.* (1995). The opposite tendency for patchy saturation at ultrasonic frequencies is also consistent with the observation of Cadoret *et al.* (1995) for Estaillades limestone. For the patchy saturated 'mean' Berea sandstone data of King *et al.* (2000), used as our model rock, the similarity is obvious and the small mismatch can, in general, be attributed to the higher frequencies (500–900 kHz) applied by King *et al.* (2000).

Also, the P-wave attenuation versus S_w, commonly expressed by the inverse quality factor $Q_{P_+}^{-1}$ shown in Fig. 9, displays the characteristic features of White's (1975) model and published experimental data, with low attenuation when the rock is fully saturated with gas or water, respectively, and higher attenuation at intermediate values of S_w, and with a
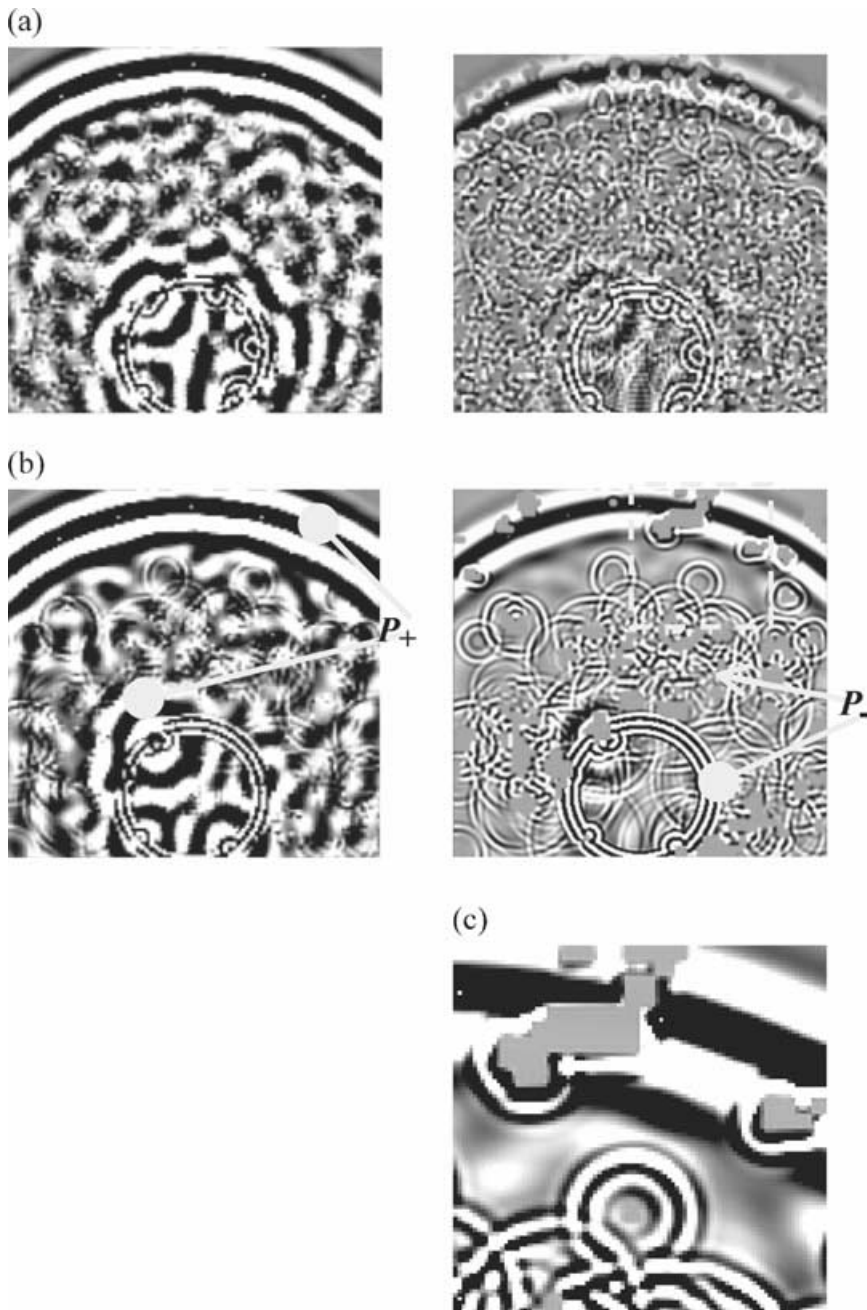
peak attenuation when approaching 100% water saturation. In general, $Q_{P_+}^{-1}$ in the uniform models is higher than that of the patchy saturation model by a factor of nearly two. The reason for the latter becomes obvious when comparing the different levels of slow-wave intensity apparent from the snapshots in Figs 6 and 7. Since the quasi-static slow waves dissipate over a much shorter distance than the fast waves and since the slow waves extract energy from the primary wavefield, this

mode conversion constitutes an efficient loss mechanism. Apparently, the more secondary slow waves are generated, the greater the loss of primary P-wave energy. Since the wavelength of slow waves is much smaller (1–15%) than for the fast waves (1 mm and 7 mm at 500 kHz, 4 mm and 340 mm at 10 kHz), small-scale heterogeneities, far below the wavelength of the fast wave, may be equally important in the loss of the primary wavefield. The population density of saturation

**Figure 7** Same properties as in Fig. 6 but for $f = 250$ kHz.
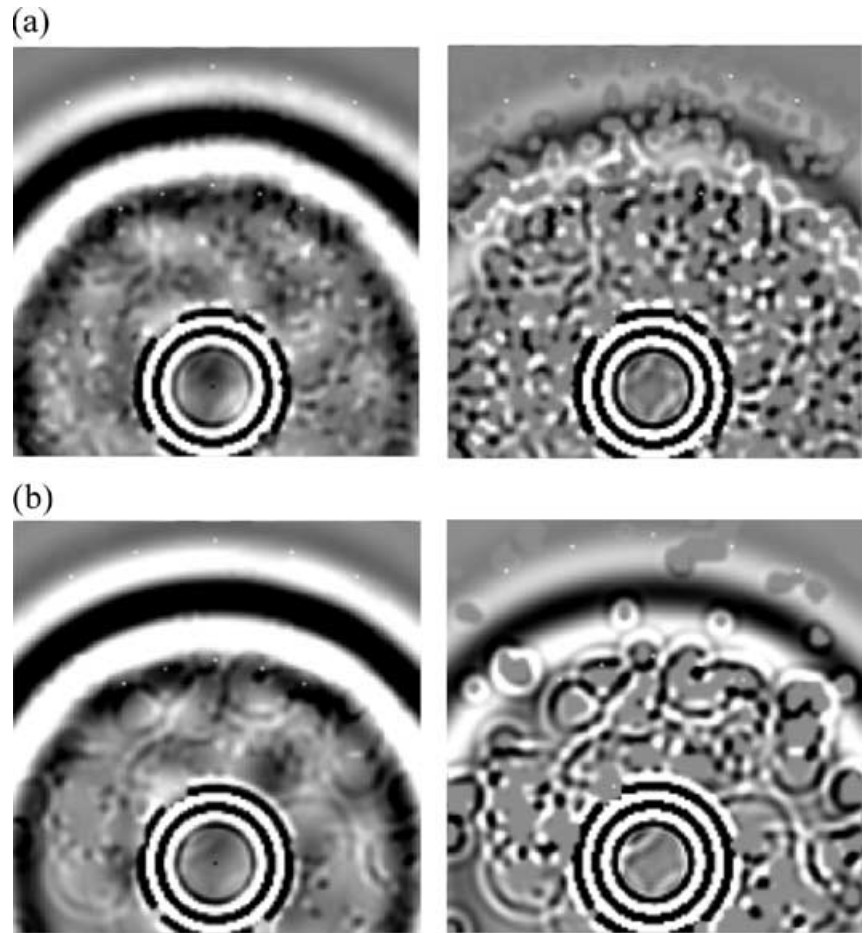
heterogeneities, not their size, thus seems to be the key factor in attenuating the primary wavefield.

CRITICAL BEHAVIOUR OF THE POROELASTIC WAVEFIELD

As has been well established from White's (1975) theory and laboratory data, the attenuation is strongly dependent on S_w and frequency f. A consistent feature apparent from Fig. 9 is the shift in the attenuation peaks towards higher S_w with decreasing f. While the 500 kHz wave in the uniform model has its attenuation peak for $S_w = 0.6$, the 10 kHz wave has its attenuation peak at $S_w = 0.98$. Maximum attenuation occurs for $f = 125$ kHz at $S_w = 0.95$. It appears that a resonance phenomenon exists around 100 kHz as shown by the three snapshots of fluid pressure shown in Fig. 10. Here the small-scale pressure perturbations in the tail of the primary wavefront are insignificant at $S_w = 0.6$ but increase to a high intensity and amplitude at $S_w = 0.9$, indi-cating remarkably strong pressure variations (and fluid flow) at a scale much smaller than the wavelength of the primary wavefield. Experimentally, such peaks in attenuation are frequently observed. They include peaks in attenuation versus permeability (Klimentos and McCann 1990; Akbar, Dvorkin and Nur 1993), versus frequency and viscosity (Murphy, Winkler and Kleinberg 1986; Jones 1986; Vo-Thanh 1990), versus porosity (Ogushwitz 1985) and versus saturation (Winkler and Nur 1979; Murphy 1982; Yin *et al.* 1992; Cadoret *et al.* 1998).

Viscoelastic materials respond to wave excitation differently, depending on the frequency of the wave. At low frequencies, fluid is relaxed causing a small induced fluid pressure. At high frequencies, fluid is unrelaxed and the induced fluid pressure is large. At an intermediate crossover frequency, a transition from relaxed to unrelaxed mode occurs. This transition frequency, separating the relaxed and unrelaxed states, that is, the location of the relaxation peak, is approximately given by White's (1975) theory,
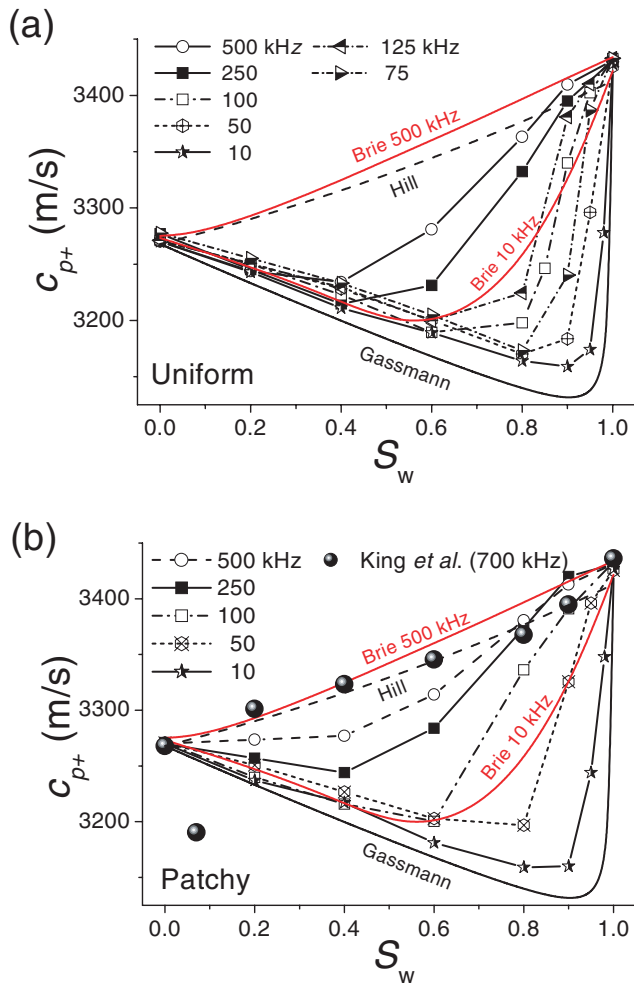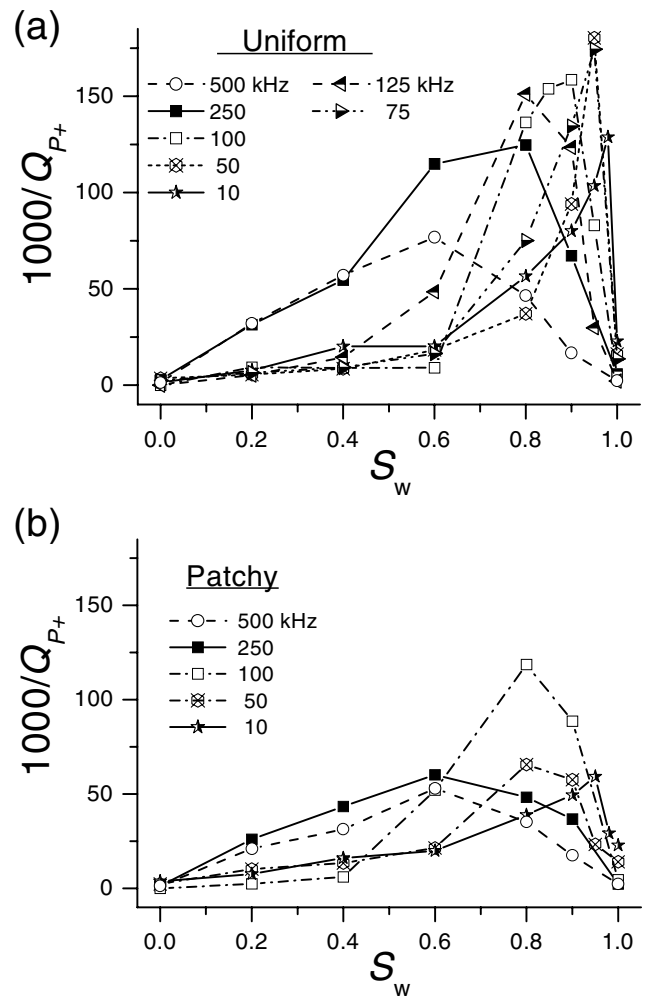
Figure 8 P-wave velocity versus water saturation as a function of frequency determined from the numerical simulation in (a) uniform and (b) patchy models. The models of Hill, Gassmann and the modified Brie *et al.* (Pham *et al.* 2002) and the data of King *et al.* (2000) are shown for comparison.

Figure 9 P-wave attenuation factor versus water saturation as a function of frequency determined from the numerical simulation in (a) uniform and (b) patchy models. Note the marked peaks around $S_w = 0.9$ at 50–125 kHz for the uniform models.

$$f_c = \frac{\kappa K_{E2}}{\pi \eta_2 (b-a)^2}, \qquad (11)$$

where a and b are radii of the inner and outer spheres, respectively, in White's model, κ is the permeability, K_{E2} is an effective bulk modulus of the water-filled rock (e.g. Mavko *et al.* 1998, p. 208) and η_2 is the viscosity of water. Dutta and Seriff (1979) considered b^2, instead of $(b-a)^2$, in the denominator. However, as pointed out by Carcione *et al.* (2003), the relevant relaxation distance should be the thickness of the outer shell, i.e. $(b-a)$.

The gas saturation is given by $S_g = 1 - S_w = (a/b)^3$ (White 1975), and assuming a constant gas-pocket radius a, the crit-

ical saturation is given by

$$S_{wc} = 1 - \left(1 + \sqrt{\frac{\kappa K_{E2}}{\pi \eta_2 f a^2}}\right)^{-3}, \qquad (12)$$

showing that the peak attenuation is located at low values of S_w for the high-frequency range and vice versa, which is in qualitative agreement with the results given in Fig. 9. Since (11) has the form of the length-squared dependency characteristic of diffusion phenomena, we define a critical length scale,
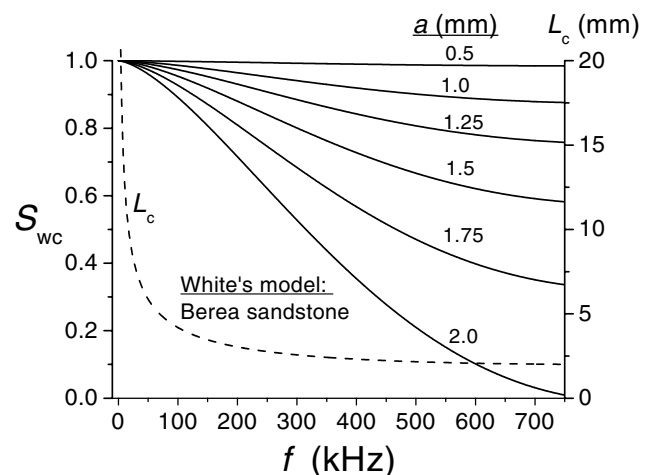
$$L_c \approx \left(\frac{\kappa K_{E2}}{\pi \eta_2 f}\right)^{1/2} = (b_c - a), \qquad (13)$$
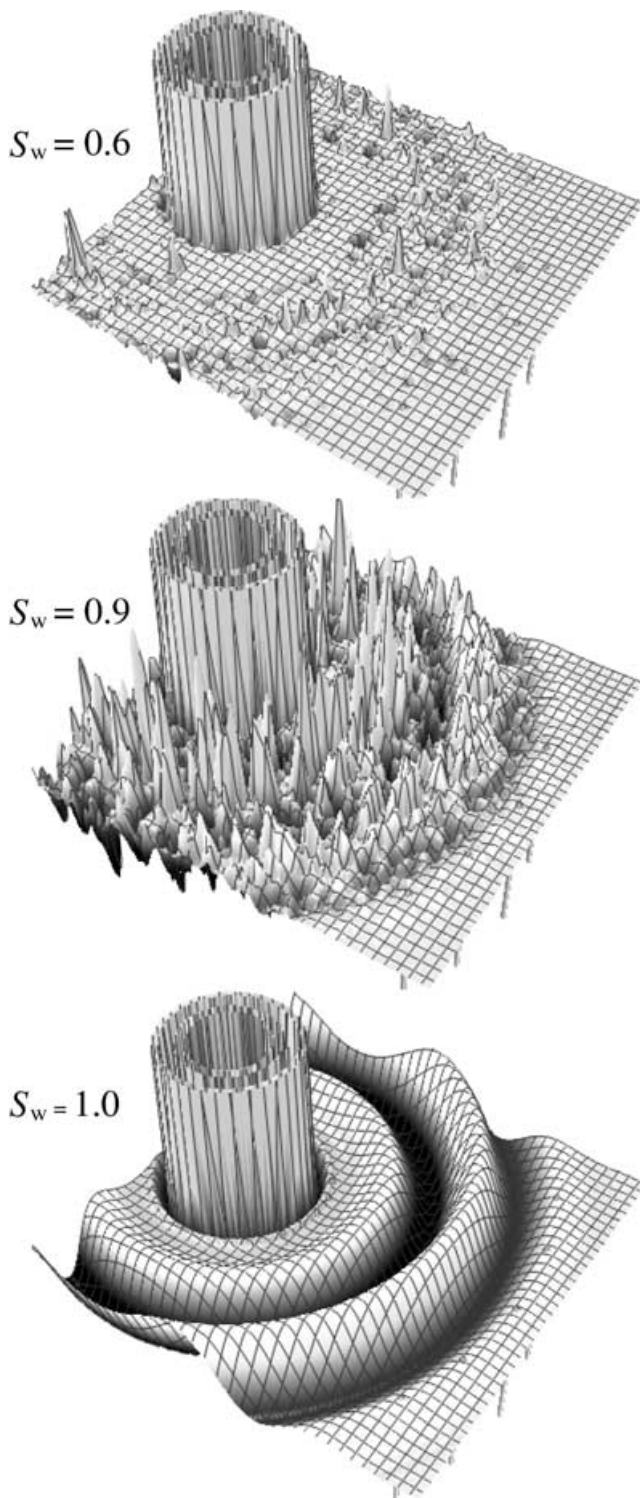
where b_c is the critical value of b with a fixed, suggesting that during a seismic period the pore pressure can equilibrate over a spatial scale smaller than L_c, corresponding to the distance over which the slow wave propagates/diffuses away from a gas–fluid interface (e.g. Johnson 2001). This state assumes a fine-scale, uniform distribution of fluids, which is equivalent to our uniform models. In contrast, saturations that are heterogeneous over scales larger than L_c have wave-induced pore-pressure gradients that cannot equilibrate. This state is referred to as patchy saturation. Critical saturation scales are typically 1–10 mm for laboratory measurements and tens of centimetres for field seismic frequencies (Mavko and Mukerji 1998). Critical saturation and relaxation scale versus frequency, obtained from White's model, are shown in Fig. 11. Using the material properties from Table 1, the relaxation peaks appear close to $S_w = 1$ and their locations are almost independent of frequency for $a = 0.5$ mm. For $a = 2$ mm, the location of S_{wc} is very sensitive to frequency, starting at $S_{wc} = 1$ for $f = 0$ and rapidly decreasing to $S_{wc} = 0$ at about 800 kHz. According to (13), the relaxation scale L_c is dependent only on the rock and fluid properties, and decreases rapidly from several centimetres within the seismic frequency band to about 2 mm in the ultrasonic range.

From (11), it follows that the permeability κ and critical frequency f_c are linearly related, i.e. increasing permeability causes the relaxation peak to move towards higher frequencies. We have seen (Figs 9 and 10) that the relaxation peaks in S_w are well expressed in the poroelastic simulation and are in

Figure 10 Perspective view of snapshots at 300 time steps showing the fluid pressure field for the uniform model with saturations $S_w = 0.6$, 0.9 and 1.0. Note the critical behaviour at $S_w = 0.9$. The central frequency is 100 kHz.

Figure 11 Critical water saturation S_{wc} (solid line) and relaxation scale L_c (dashed line) as a function of wave frequency f for a range of values of the radius a (in mm) of the gas spheres (patches) in White's model. Material and fluid properties as given in Table 1.
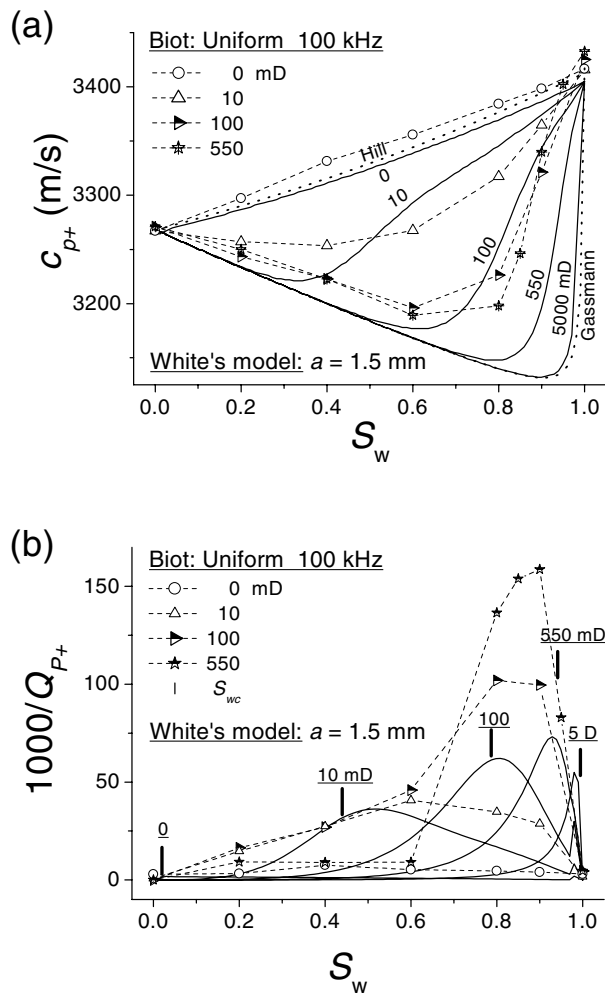
Figure 12 P-wave velocity (a) and attenuation factor (b) versus water saturation for a range of permeabilities and a fixed frequency of 100 kHz. The solid lines are the corresponding values from White's model with gas pockets of constant diameter $a = 1.5$ mm. Vertical bars indicate critical saturations computed from (12). The models of Hill and Gassmann are shown for comparison.

agreement with (12) for the range of wave frequencies f and for a constant permeability $\kappa = 550$ mD. Changes in velocity with frequency are a common experience. Changes in velocity with permeability have been paid less attention although they follow from White's (1975) theory. Figure 12 shows velocity and attenuation as a function of S_w and permeability. Here, we fix the frequency at 100 kHz and vary the permeability. The effect of permeability on velocity is significant and covers approximately the same envelope as that of varying the frequency (Fig. 8a) with constant permeability. For $\kappa = 0$, the velocity coincides with the high-frequency upper bound

(Hill's average) and for $\kappa = 5000$ mD, it coincides with the lower bound (Gassmann).

Velocity and attenuation from the poroelastic simulation reveal similarity with those of White's theory for fixed $a = 1.5$ mm. The locations of the relaxation peaks are reasonably well predicted by White's theory and equation (12). However, the level of attenuation predicted by White's theory is, in general, less than that of poroelastic simulations, as also shown by Carcione *et al*. (2003) for a regular distribution of circular gas pockets.

HETEROGENEITIES IN ROCK MATERIAL VERSUS FLUID DISTRIBUTION

Heterogeneity of the rock material has also been an important factor in explaining the observed behaviour of elastic waves in rocks. Blair (1990) compared experimental attenuation measured in two frequency ranges (1–150 kHz and 1–50 kHz) on a dry granite block and concluded that grain clusters of the size (~10 mm) comparable to the wavelength rather than grains (~1 mm) themselves were responsible for the large ultrasonic attenuation. Supported by X-ray scans of the rock samples, Lucet and Zinszner (1992) showed similar results from sonic and ultrasonic laboratory data in saturated limestone, containing significant material heterogeneities. They suggested that scattering (diffraction) of the waves at the heterogeneities could be an additional mechanism for attenuating the primary wavefield in the case of limestone. However, this mechanism occurs mainly at ultrasonic frequencies when the wavelength is comparable to the size of the heterogeneities. On the other hand, sandstone samples with more smoothly varying rock properties exhibit, in general, less ultrasonic attenuation. In the experiment shown in Figs 13 and 14, we investigate this phenomenon by substituting the gas with inclusions of low-velocity grain material ($K_i = 24.4$ GPa embedded in a background of 35 GPa) such that P-wave impedance contrasts are approximately the same as in the case of gas inclusions. The fractal distributions are identical with those of the corresponding gas–fluid models (Figs 1 and 2) and the rock is fully saturated with water.
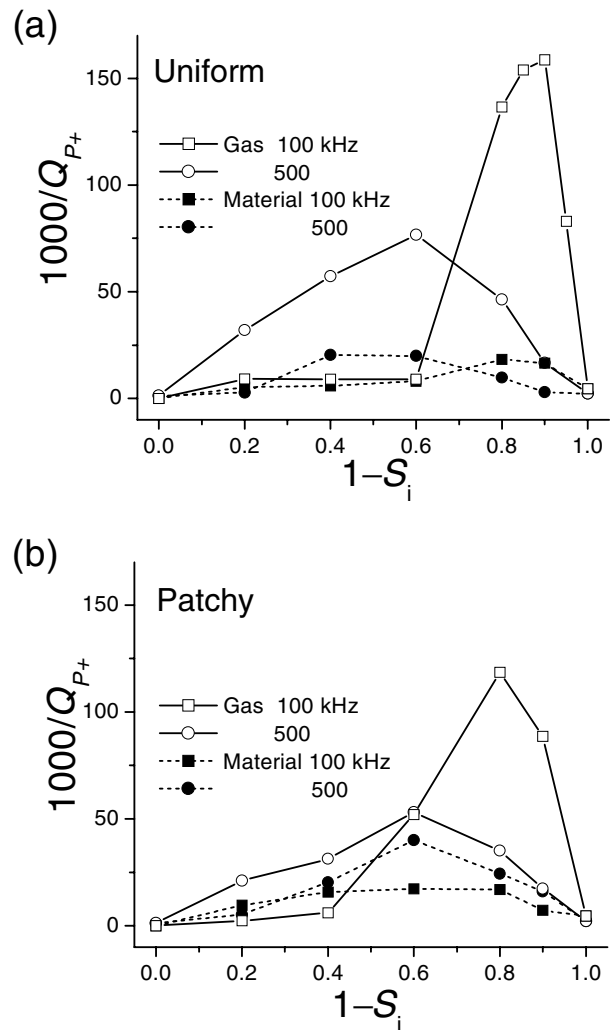
We display the results for 100 kHz and 500 kHz and compare them with the corresponding models containing gas inclusions. Firstly, in the case of material inclusions there is minor velocity dispersion and negligible response to the patch size, compared with those of gas inclusions (Fig. 13). For attenuation (Fig. 14), on the other hand, we find a significant response to both frequency and patch size. Moreover, the relaxation peaks for material and gas inclusions coincide, indicating that
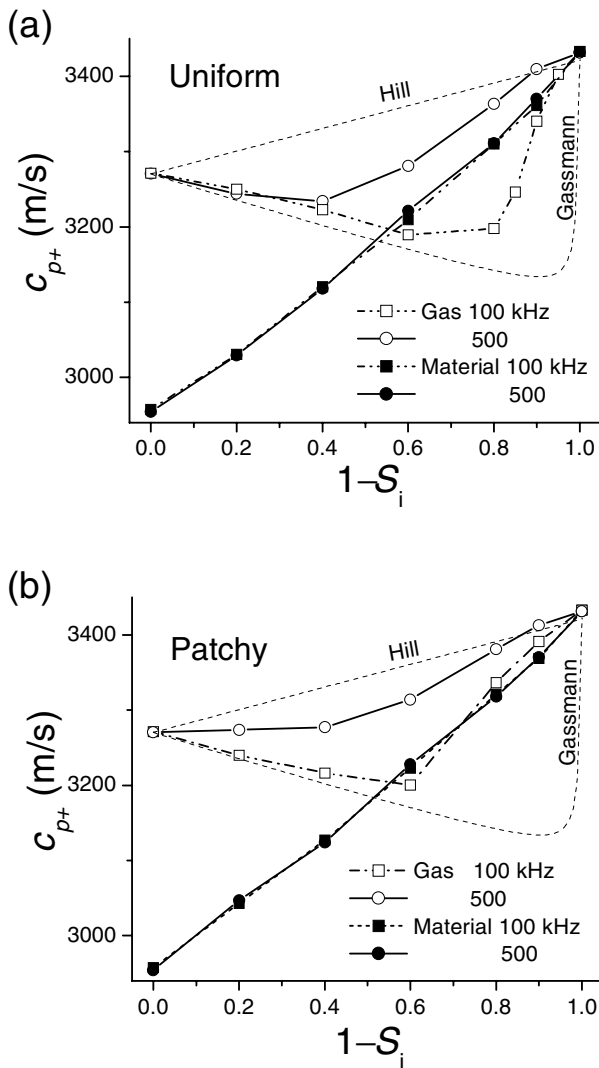
Figure 13 P-wave velocity versus gas or material inclusion S_i in a water-saturated background determined from numerical simulation in (a) uniform and (b) patchy models.

Figure 14 P-wave attenuation factor versus gas or material inclusion S_i in a water-saturated background determined from numerical simulation in (a) uniform and (b) patchy models.

the same attenuation mechanism is active in the two models. For the magnitude of attenuation, the effects of patch size are opposite: while small gas patches (uniform model) favour high attenuation, the larger patch size (patchy model) seems more favourable in the case of material inclusions, in particular at 500 kHz when the wavelength of the primary wave ($\lambda \sim$ 5 mm) coincides with the dominant patch size (Fig. 2).

Heterogeneity in permeability is a related problem. We have shown (Fig. 12) that in a fully saturated rock (gas or water) the permeability has minor effects on the wavefield. On the other hand, by introducing a small fraction of gas into water-saturated rocks, the permeability becomes a key parameter.

The observation of patchy distribution of permeability, apparent in cores and well logs (Helle, Bhatt and Ursin 2001), has led us to introduce the following model: The background model is the porous rock (Table 1) with an effective water saturation $S_w = 0.9$ where the water/gas is distributed according to the uniform model. Superimposed on the uniform fluid heterogeneities, we introduce the patchy model for permeability, using the binary values of 2 mD and 2000 mD, respectively, to cover the range of effective permeabilities in a real reservoir. This experiment mimics a realistic situation where the rock contains a small fraction of gas (10%) uniformly distributed throughout the matrix at a fine scale, but where patches of calcite-cemented grains control the effective permeability at

(a)

(b)
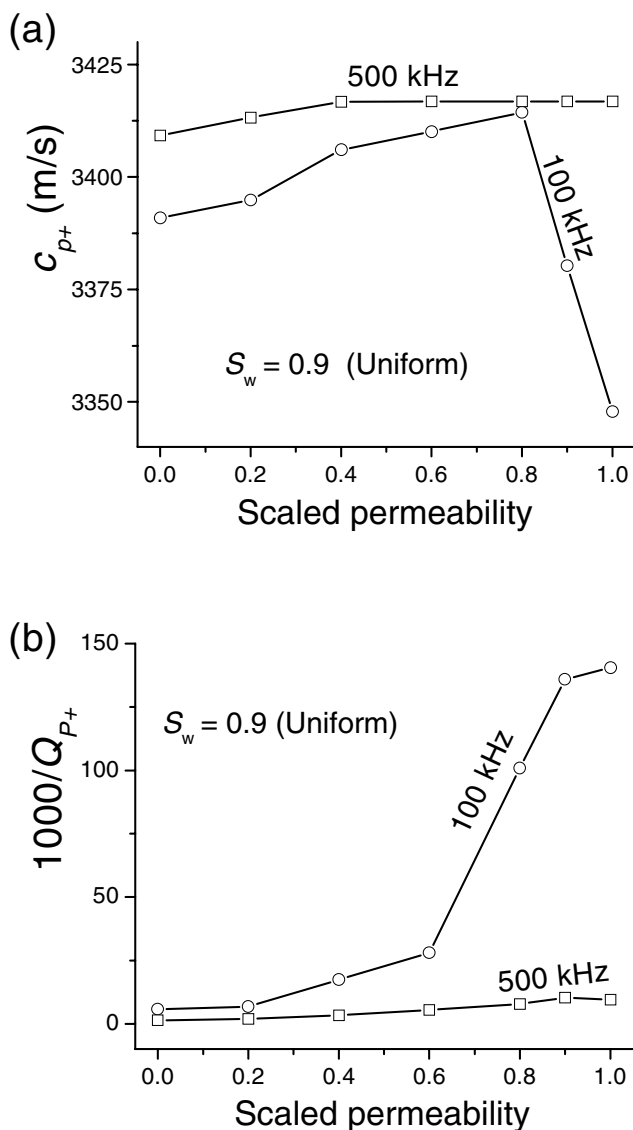
Figure 15 (a) P-wave velocity and (b) attenuation factor versus scaled permeability (2–2000 mD) in a uniform fluid model of $S_w = 0.9$ and a patchy permeability distribution using 2000 mD patches in a background rock of 2 mD.

a coarser scale. Starting with a model of homogeneous permeability of 2 mD, we gradually add permeability patches of 2000 mD until the rock attains a homogeneous permeability of 2000 mD. The resulting velocity-attenuation pairs obtained from the poroelastic simulation are shown in Fig. 15. For 100 kHz, there is a strong response in velocity and attenuation due to the permeability patches, as may be expected from the results shown in Fig. 12 where the response to permeability is at its maximum around $S_w = 0.9$. The response

is comparable in magnitude to the case of partial saturation. For higher frequencies (500 kHz), the response is weak with a slow monotonic increase in velocity and attenuation with increasing effective permeability.

The snapshots of the fluid pressure for the three alternative inclusions (Fig. 16) reveal that slow waves are generated at the heterogeneities in all cases, but to varying degrees. Slow-wave generation thus seems to be an important factor for any type of heterogeneity in a fluid-filled porous rock, and is particularly effective in the presence of gas. Gas inclusions are the most effective slow-wave exciters, whereas material inclusions in the case of full water saturation are less efficient. The effects of permeability patches are of great practical significance and therefore deserve a more detailed evaluation and discussion in a separate paper. However, from the simple experiments above, we conclude that patches in the permeability give a strong response in the lower end of the ultrasonic band, and probably also at sonic frequencies.

CONCLUSIONS

Seismic wave propagation in porous rocks depends not only on the degree of saturation but also on the distribution of the fluid phase and rock properties at various scales. In the present study, we have applied a numerical solution of Biot's poroelastic differential equation to simulate the wavefield in a porous rock partially saturated with water and gas. Two fractal distributions of the fluid are designed to match published laboratory experiments: uniform distribution of small-scale patches, corresponding to variation of saturation by depressurization, and large-scale patches, characteristic of the drainage by drying. We record and analyse the transmitted wave with respect to P-wave velocity and attenuation in the frequency range 10–500 kHz as a function of effective partial saturation. Without resorting to additional phenomenological matrix–fluid interaction mechanisms (e.g. squirt flow), we are able to reproduce the main features of published experiments on velocity and attenuation of P-waves in partially saturated rocks.

Peaks in attenuation versus saturation are linked with a crossover frequency, from relaxed to unrelaxed mode, determined by the hydraulic properties of the host rock, the properties of the viscous fluids and the fluid distribution within the rock matrix. The observed critical saturation from the poroelastic simulation is in qualitative agreement with White's (1975) theory and is equivalent to the observations of attenuation peaks as a function of viscosity, permeability and porosity. However, the level of attenuation estimated from the poroelastic modelling exceeds that predicted by White's theory, in
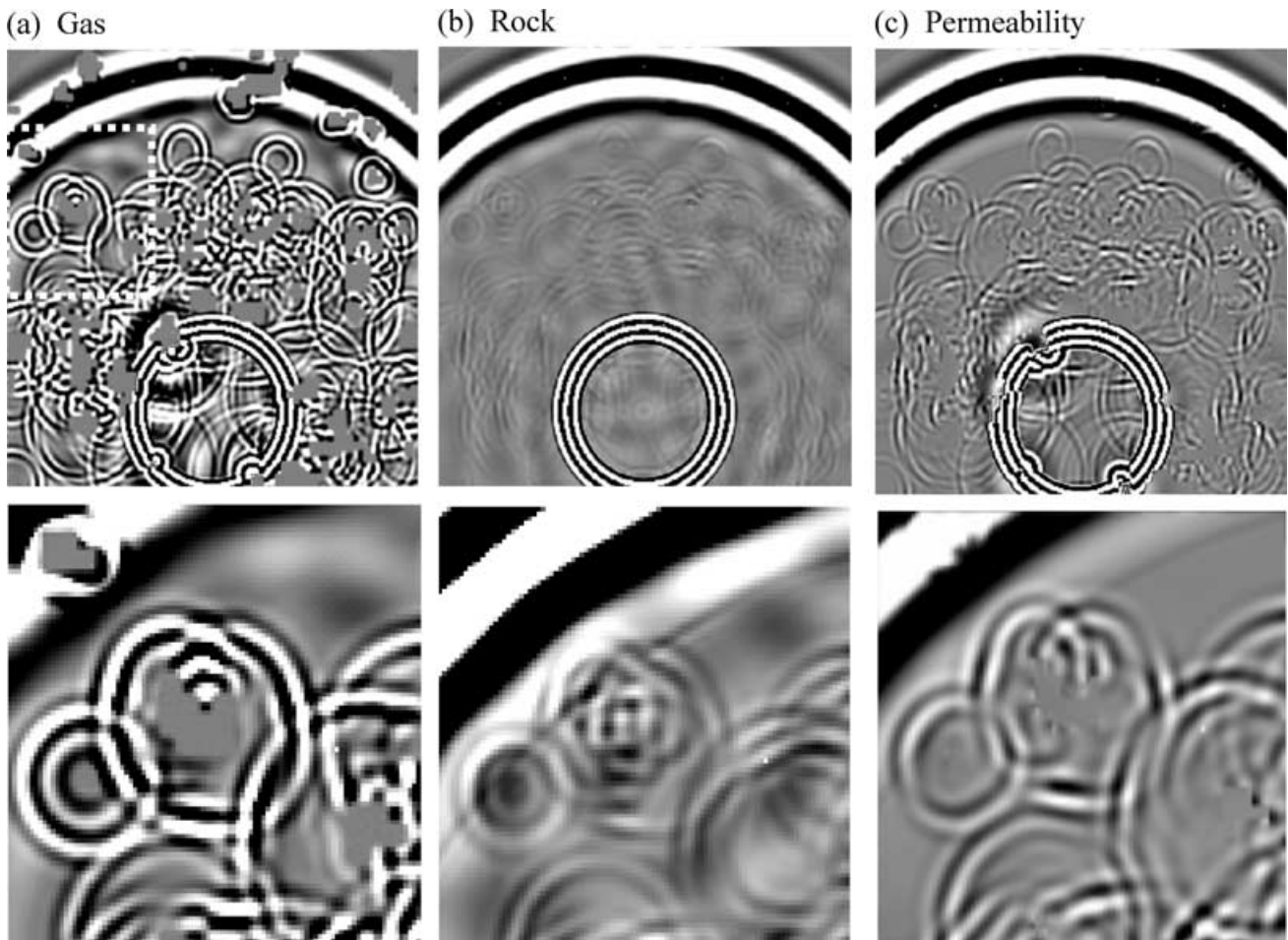
Figure 16 Snapshots after 300 time steps (18.6 μs) of the fluid pressure for the patchy saturation for $S_g = 0.1$ (a), the equivalent distribution of solid inclusions (b) and permeability inclusions (c) in a fully water-saturated rock ($f = 500$ kHz). The lower pictures show details of slow-wave conversion at the inclusion patches.

agreement with the results of Carcione *et al.* (2003) for a regular distribution of gas pockets.

We have shown that the conversion of primary P-wave energy into dissipating slow waves at heterogeneities in the fluid and rock properties is the main mechanism for the observed P-wave attenuation. Inclusions of gas are far more efficient slow-wave exciters than inclusions of rock material, and hence more attenuation is observed for gas inclusions than for the equivalent inclusions of rock material. While the uniform model is the most effective in the case of fluid heterogeneities, the patchy model is more effective in the case of rock inclusions when the size of the inclusions is comparable with the wavelength.

Since a patchy distribution of permeability represents an important practical problem, we have included a limited study in this paper. With a small portion of gas in the pore-fill, the wave response becomes very sensitive to permeability, and to the permeability distribution. Experimental results indicate minor effects at ultrasonic frequencies but a strong response in the sonic band.

REFERENCES

Akbar N., Dvorkin J. and Nur A. 1993. Relating P-wave attenuation to permeability. *Geophysics* **58**, 20–29.

Biot M.A. 1962. Mechanics of deformation and acoustic propagation in porous media. *Journal of Applied Physics* **33**, 1482–1498.

Blair D.P. 1990. A direct comparison between vibrational resonance and pulse transmission data for assessment of seismic attenuation in rock. *Geophysics* **55**, 51–60.

Bourbie T. and Zinszner B. 1984. Saturation methods and attenuation versus saturation relationships in Fontainebleau sandstone. 54th SEG meeting, Atlanta, USA, Expanded Abstracts, 344–347.

Brie A., Pampuri F., Marsala A.F. and Meazza O. 1995. Shear sonic interpretation in gas-bearing sands. Society of Petroleum Engineers, Annual Technical Conference, Dallas, USA, (Paper # 30595), 701–710.

Cadoret T., Marion D. and Zinszner B. 1995. Influence of frequency and fluid distribution on elastic wave velocities in partially saturated limestones. *Journal of Geophysical Research* **100**(B6), 9789–9803.

Cadoret T., Mavko G. and Zinszner B. 1998. Fluid distribution effect on sonic attenuation in partially saturated limestones. *Geophysics* **63**, 154–160.

Carcione J.M. 1996. Wave propagation in anisotropic, saturated porous medium: plane-wave theory and numerical simulation. *Journal of the Acoustical Society of America* **99**(5), 2655–2666.

Carcione J.M. 2001. *Wave Fields in Real Media: Wave Propagation in Anisotropic, Anelastic and Porous Media*. Handbook of Geophysical Exploration, Vol. 31. Pergamon Press Inc.

Carcione J.M. and Helle H.B. 1999. Numerical simulation of the poro-viscoelastic wave equation on a staggered mesh. *Journal of Computational Physics* **154**, 520–527.

Carcione J.M., Helle H.B. and Pham N.H. 2003. White's model for wave propagation in partially saturated rocks: comparison with poroelastic numerical experiments. *Geophysics* **68**, 1389–1398.

Carcione J.M., Quiroga-Goode G. and Cavallini F. 1996. Wavefronts in dissipative anisotropic media: comparison of the plane wave theory with numerical simulations. *Geophysics* **61**, 857–861.

Domenico S.N. 1977. Elastic properties of unconsolidated porous sand reservoirs. *Geophysics* **42**, 1339–1368.

Dutta N.C. and Seriff A.J. 1979. On White's model of attenuation in rocks with partial gas saturation. *Geophysics* **44**, 1806–1812.

Frankel A. and Clayton R.W. 1986. Finite difference simulation of seismic wave scattering: implications for the propagation of short period seismic waves in the crust and models of crustal heterogeneity. *Journal of Geophysical Research* **91**, 6465–6489.

Gassmann F. 1951. Über die elastizität poröser medien. *Vierteljahrsschrift der Naturforschenden Gesellschaft in Zürich* **96**, 1–23.

Gist G.A. 1994. Interpreting laboratory velocity measurements in partially gas-saturated rocks. *Geophysics* **59**, 1100–1109.

Gregory A.R. 1976. Fluid saturation effects on dynamic elastic properties of sedimentary rocks. *Geophysics* **41**, 895–921.

Helle H.B., Bhatt A. and Ursin B. 2001. Porosity and permeability prediction from wireline logs using artificial neural networks: a North Sea case study. *Geophysical Prospecting* **49**, 431–444.

Holliger K. 1997. Seismic scattering in the upper crystalline crust based on evidence from sonic logs. *Geophysical Journal International* **128**, 65–72.

Johnson D.L. 2001. Theory of frequency dependent acoustics in patchy-saturated porous media. *Journal of the Acoustical Society of America* **110**(2), 682–694.

Jones T.D. 1986. Pore fluids and frequency-dependent wave propagation in rocks. *Geophysics* **51**, 1939–1953.

King M.S., Marsden J.M. and Dennis J.W. 2000. Biot dispersion for P- and S-wave velocities in partially and fully saturated sandstones. *Geophysical Prospecting* **48**, 1075–1089.

Klimentos T. and McCann C. 1990. Relationships among compressional wave attenuation, porosity, clay content, and permeability in sandstones. *Geophysics* **55**, 998–1014.

Knight R. and Nolen-Hoecksema R. 1990. A laboratory study of the dependence of elastic wave velocities on pore scale fluid distribution. *Geophysical Research Letters* **17**, 1529–1532.

Lucet N. and Zinszner B. 1992. Effects of heterogeneities and anisotropy on ultrasonic attenuation in rocks. *Geophysics* **57**, 1018–1026.

Mavko G. and Mukerji T. 1998. Bounds on low-frequency seismic velocities in partially saturated rocks. *Geophysics* **63**, 918–924.

Mavko G., Mukerji T. and Dvorkin J. 1998. *The Rock Physics Handbook: Tools for Seismic Analysis in Porous Media*. Cambridge University Press.

Murphy W.F. 1982. Effect of partial water saturation on attenuation of Massilon sandstone and Vycor porous glass. *Journal of the Acoustical Society of America* **71**, 1458–1468.

Murphy W.F. 1984. Acoustic measures of partial gas saturation in tight sandstones. *Journal of Geophysical Research* **89**, 11549–11559.

Murphy W.F., Winkler K.W. and Kleinberg R.L. 1986. Acoustic relaxation in sedimentary rocks: dependence on grain contacts and fluid saturation. *Geophysics* **51**, 757–766.

O'Connell R.J. and Budiansky B. 1977. Viscoelastic properties of fluid-saturated cracked solids. *Journal of Geophysical Research* **82**, 5719–5735.

Ogushwitz P.R. 1985. Application of the Biot theory. II. Suspension. *Journal of the Acoustical Society of America* **77**, 441–452.

Pham N.H., Carcione J.M., Helle H.B. and Ursin B. 2002. Wave velocities and attenuation of shaley sandstones as a function of pore pressure and partial saturation. *Geophysical Prospecting* **50**, 615–627.

Toksöz M.N., Johnston D.H. and Timur A. 1979. Attenuation of seismic waves in dry and saturated rocks: I. Laboratory measurements. *Geophysics* **44**, 681–690.

Tserkovnyak Y. and Johnson D.L. 2002. Can one hear the shape of a saturation patch? *Geophysical Research Letters* **29**, 1–4.

Vo-Thanh D. 1990. Effects of fluid viscosity on shear-waves attenuation in saturated sandstones. *Geophysics* **55**, 712–722.

White J.E. 1975. Computed seismic speeds and attenuation in rocks with partial saturation. *Geophysics* **40**, 224–232.

Winkler K.W. and Nur A. 1979. Pore fluids and seismic attenuation in rocks. *Geophysical Research Letters* **6**, 1–4.

Winkler K.W. and Nur A. 1982. Seismic attenuation: effects of pore fluids and frictional sliding. *Geophysics* **47**, 1–15.

Yin C.-S., Batzle M.L. and Smith B.J. 1992. Effects of partial liquid/gas saturation on extensional wave attenuation in Berea sandstone. *Geophysical Research Letters* **19**, 1399–1402.